ACS Catalysis
Research Article
pubs.acs.org/acscatalysis

Positive Effects of K^+ Ions on Three-Dimensional Mesoporous Ag/Co_3O_4 Catalyst for HCHO Oxidation

Bingyang Bai[†] and Junhua Li*,[†,‡]

[†]State Key Joint Laboratory of Environment Simulation and Pollution Control, School of Environment, Tsinghua University, Beijing 100084, China

[‡]State Environmental Protection Key Laboratory of Sources and Control of Air Pollution Complex, Beijing 100084, China

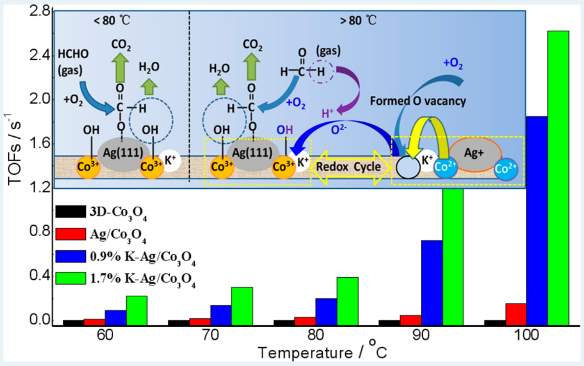

ABSTRACT: Three-dimensional (3D) ordered mesoporous Ag/Co_3O_4 and K−Ag/Co_3O_4 catalysts were successfully prepared on the basis of 3D-Co_3O_4. All catalysts possess 3D mesoporous structures, which are not affected due to Ag and K addition. Ag nanoparticles, uniformly dispersed and supported on the polycrystalline wall of K−Ag/Co_3O_4, provide sufficient active sites for HCHO oxidation reaction. 1.7% K−Ag/Co_3O_4 has turnover frequencies (TOFs) of 0.22 s^{-1} at 60 °C and 2.62 s^{-1} at 100 °C, and its HCHO conversion at room temperature is 55% (HCHO 100 ppm and GHSV 30000 h^{-1}). The addition of K^+ ions obviously promotes the catalytic performance for HCHO oxidation due to surface OH^- species provided by K^+ ions and more abundant Ag(111) active faces, Co^{3+} cations and surface lattice oxygen (O^{2-}) species generated by stronger interaction between Ag and Co and anion lattice defects. Ag(111) faces, Co^{3+} ions, and O^{2-} are active species. Combined with TOFs, at low temperature (<80 °C), the HCHO catalytic activity on K−Ag/Co_3O_4 catalyst largely depends on the surface OH^- species at the perimeter of the Ag(111) facets; at relatively high temperature (>80 °C), the surface OH^- species are consumed and replaced quickly, and their supplement relies on the migration of O^{2-} species from 3D-Co_3O_4 support. The pathway of reaction for HCHO oxidation on the K−Ag/Co_3O_4 follows the HCHO → $CHOO^-$ + OH^- → CO_2 + H_2O route.

KEYWORDS: *three-dimensional mesoporous, Co_3O_4, HCHO oxidation, silver, potassium ions*

1. INTRODUCTION

Formaldehyde (HCHO) emitted from widely used building and decorative materials, oil paints, textiles, and hospitals, has photochemical activity in the atmosphere.[1] It is one of the most dominant air pollutants in an indoor environment.[2] Long-term exposure to indoor air containing even a few parts per milion of HCHO may lead to serious and hazardous effects on human health. Thus, great efforts have been made to reduce the indoor emission of HCHO for satisfying stringent environmental regulations.[3,4] Conversional absorbing materials have beenused to eliminate HCHO emission, but the efficiency of removal has not been excellent because of the limited capacities.[4] Catalytic oxidation is a better method to remove HCHO, but the key is the choice of catalytic materials. Currently, the catalytic materials used in catalytic oxidation of HCHO are mainly oxide-supported noble metal (Pt, Pd, Au an Ag) catalysts, such as Pt/MnO_x−CeO_2,[3] Pt/TiO_2,[4−7] Pt/MnO_2,[8] Pt/Fe_2O_3,[9] Pt/SiO_2,[10] Pd/TiO_2,[11] Pd/Beta,[12] Pd−Mn/Al_2O_3,[13] Au/CeO_2,[14−16] Au/Fe_2O_3,[17] Au/ZrO_2,[18] Au/Co_3O_4−CeO_2,[19] Au/CeO_2−Co_3O_4,[20] Ag/SBA-15,[21] Ag/HMO,[22] Ag/SiO_2,[23] Ag/CeO_2,[24] Ag/MnO_x-CeO_2,[25] etc. In addition, several metal oxide catalysts for the oxidation of HCHO, such as K_xMnO_2,[26] Co/Zr,[27] and mesoporous Co−Mn,[28] Cr_2O_3[29] and 3D-Co_3O_4,[30] etc., have been reported. Compared with metal oxide catalysts, oxide-supported noble metal catalysts can provide sufficient noble metal active sites for the oxidation of HCHO, and they have better HCHO catalytic activity at low temperature, probably attributed to the interaction of the metal with the support. However, these catalysts would not possess excellent catalytic activities of HCHO at much lower temperature if precious metal were not added.

In recent years, more attention has been paid to mesoporous metal oxides because of their special pore structure, large surface area, controllable pore diameter, and pore volume.[30−35] Interaction of a noble metal and support in oxide-supported noble metal catalysts has been proven to have an extremely beneficial effect on catalytic activity.[36−38] An et al.[39]prepared three-dimensional (3D) Pt/Co_3O_4 catalyst, which is better than other oxide-supported Pt catalysts on catalytic performance of CO oxidation, such as 3D Pt/NiO, Pt/MnO_2, Pt/CeO_2, and so on, because the interaction of Pt with Co is stronger and the interface of Pt and Co_3O_4 is the active surface phase. Ma et al.[40] reported 3D Au/Co_3O_4 had much higher catalytic activity for ethylene oxidation due to the insertion of Au into crystalline walls of Co_3O_4. The insertion probably leads to a stronger interaction of Au and Co and increases quantities of Co^{3+}

Received: May 15, 2014
Revised: June 25, 2014
Published: July 3, 2014

dx.doi.org/10.1021/cs5006663 | *ACS Catal.* 2014, 4, 2753−2762

cations exposed on the (110) crystal planes and surface active oxygen species, which are favorable for the oxidation reaction. Liu et al.[41] also reported 3D Au/Co_3O_4 has excellent oxidation performance for carbon monoxide, benzene, toluene, and *o*-xylene because of a higher surface area, more oxygen adspecies, and stronger interaction between Au and Co.

At present, the development of effective catalysts for complete oxidation of low concentrations of HCHO at lower temperatures, even room temperature is still a challenge to be solved. Although the catalysts loading Pt nanoparticles have better HCHO catalytic activity,[4−7] the precursors of Pt nanoparticles are much more expensive than those of Ag nanoparticles. For instance, the price of Pt per gram for $H_2PtCl_6{\cdot}6H_2O$ is about 20 times more than that of Ag per gram for $AgNO_3$ on the Sigma-Aldrich website. Our previous literature has reported that 3D ordered mesoporous Co_3O_4 has more advantages (special mesoporous structure, larger surface area, and more active phase) to eliminate HCHO and can become a promising support because of complete HCHO conversion at 130 °C.[30] 3D-Co_3O_4 loading Ag nanoparticles for the catalytic performance of HCHO oxidation has not been reported. In addition, the literature has reported that alkali metal ions can promote the catalytic performance. For example, Nie et al.[42] reported that the addition Na^+ ions into Pt/TiO_2 can promote the catalytic activity of HCHO oxidation. Avgouropoulos et al.[43] prepared K-promoted Pt/Al_2O_3 catalyst, which enhanced the oxidation activity of ethanol at low temperature and is better than Na-promoted Pt/Al_2O_3. Hence, we would like to choose alkali metal K^+ ions as an accessory ingredient to improve HCHO oxidation activity of Ag/Co_3O_4 catalyst and analyze the effect of K^+ ions for Ag/Co_3O_4 catalyst.

In this work, 3D mesoporous Ag/Co_3O_4 catalyst was prepared by an excessive impregnation method on the basis of 3D-Co_3O_4. The K^+ ions as accessory an ingredient were added to Ag/Co_3O_4 to prepare the K−Ag/Co_3O_4 catalyst. The interaction of the noble metal and support, oxygen species and lattice defects have been proven to have extremely favorable effects on catalytic performance.[9−12] With the addition of K^+ ions, we anticipate that K−Ag/Co_3O_4 promotes a stronger interaction of Ag and Co, more lattice defects, and abundant surface active oxygen species, which can enhance the catalytic activity of HCHO. The samples are characterized by XRD, BET, TEM, H_2-TPR, CO-TPD, XPS, Raman, and in situ DRIFTS, and their catalytic activity of HCHO was evaluated.

2. EXPERIMENTAL SECTION

2.1. Catalyst Preparation. Synthesis of KIT-6 mesoporous silica and preparation of mesoporous 3D-Co_3O_4 refer to the previous literature.[30]

Preparation of mesoporous Ag/Co_3O_4 and K−Ag/Co_3O_4: 0.16 g of $AgNO_3$ was dissolved in 15 mL of ammonia−water (28 wt %) to form a silver−ammonia solution. Subsequently, 1.5 g of 3D-Co_3O_4 was added to the solution, and then 22.7 mL of H_2O_2 (30 wt %) was dropwise added with rapid stirring. The mixtures were stirred for 1 h, and centrifugal separation was used to remove the liquid phases. The samples were dried at 110 °C and calcined at 450 °C for 4 h. The Ag content was 8.2 wt % and detected by ICP-OES. The sample was marked as Ag/Co_3O_4.The preparation of different K−Ag/Co_3O_4 samples is similar to Ag/Co_3O_4. The difference was the silver−ammonia solution, which was added to K_2CO_3 (0.53 and 1.1 g). The Ag contents (6.1 and 6.4 wt %) and K contents (0.9 and 1.7 wt %) were detected by ICP-OES, and the samples were marked as 0.9% K−Ag/Co_3O_4 and 1.7% K−Ag/Co_3O_4.

2.2. Catalyst Characterization. The structural parameter, pore size distribution and N_2 adsorption isotherms of the samples were tested at liquid nitrogen temperature using an Autocorb-1MP apparatus. The samples were pretreated at 300 °C for 4 h before testing. The N_2 adsorption−desorption isotherm used the Barrett−Joyner−Halenda (BJH) method. The SEM image was taken on S-5500 instrument. The samples were prepared by ultrasonic dispersion in deionized water for 8 min and were placed on a copper grid using a capillary. XRD patterns were tested on a TTR3 type X-ray diffractometer using a Cu Kα ray radiation source. The scanning speed was 0.05°/min, tube voltage was 40 kV, and tube current was 40 mA. The 2θ of the low-angle XRD was from 0.6 to 5°, and the 2θ of the wide-angle was from 10 to 80°. TEM images were taken on a JEM-2011 instrument at a voltage of 200 kV.

The samples were prepared by ultrasonic dispersion in ethanol for 8 min and were placed on a copper grid using a capillary. The XPS patterns were measured on a PHI-5300/ESCA electronic energy spectrum at 300 W using Mg Ka X-rays as the excitation source. The data were processed by the XPS-PEAK software, and surface element contents were calculated through XPS peak areas. The inding energies (BE) of the elements were calibrated relative to the carbon impurity with a C 1s at 284.8 eV.[24] Laser Raman spectra were measured on a Renishaw Laser Raman spectrometer. Ar^+ (514.5 nm) and He−Cd lasers (325 nm) were used as the excitation source. The H_2-TPR were tested on a Chemisorb 2720 TPX apparatus; 0.05 g of samples (40−60 mesh) was pretreated in the N_2 flow at 300 °C for 1 h in a quartz reactor prior. The samples were cooled and reduced by a flow (50 mL/min) of a 10% H_2/90% Ar mixture using a temperature range of 30−900 °C with a heating rate of 10 K/min.

The H_2 consumptions of the reduction band were calibrated by a standard CuO (99.998%) powder. The characteristic number $K = S_0/FC_0$ (where S_0 is the amount of reducible species in the sample; F and C_0 are the flow and concentration of the hydrogen feed to the reactor) should be kept between 51 and 56 s, and the parameter $P = \beta S_0/FC_0$ (where β is the heating rate), between 8.5 and 9.3 K.[44,45] The CO-TPD was also tested on the above instrument. Portions (0.05 g) of samples were treated at room temperature with 50 mL/min of N_2 (5% of CO) for 1 h. The temperature was programmed to increase to 450 °C at a rate of 10 °C/min after the samples adsorbed enough CO. The in situ diffuse reflectance FTIR spectroscopy (DRIFTS) patterns were tested on a Nicolet 6700 FTIR device and scanned from 4000 to 800 cm^{-1} with 32 scans at a resolution of 4 cm^{-1}. Samples (0.05 g) were tested at 120 °C under the following conditions: 500 ppm of HCHO concentration, 150 mL/min of total flow, 20 vol % O_2, N_2 as balance gas.

2.3. Evaluation of Catalytic Activity. The catalytic oxidation of HCHO was tested in a fixed bed quartz tube reactor (Φ10 mm) with 0.2 g catalyst (40−60 mesh). HCHO gas was generated and injected using a N_2 bubbler in a low-temperature thermostatic bath at 0 °C that passed through two containers filled with formalin (an aqueous solution of 37% HCHO). The total flow rate was 100 mL/min and included 100 ppm of HCHO and 20% (vol) of O_2 balanced by N_2. The space velocity (GHSV) was 30 000 h^{-1}. The products of the reaction were detected online by an Agilent 7890A gas chromatograph with TCD and MSD connecting to Porapak-

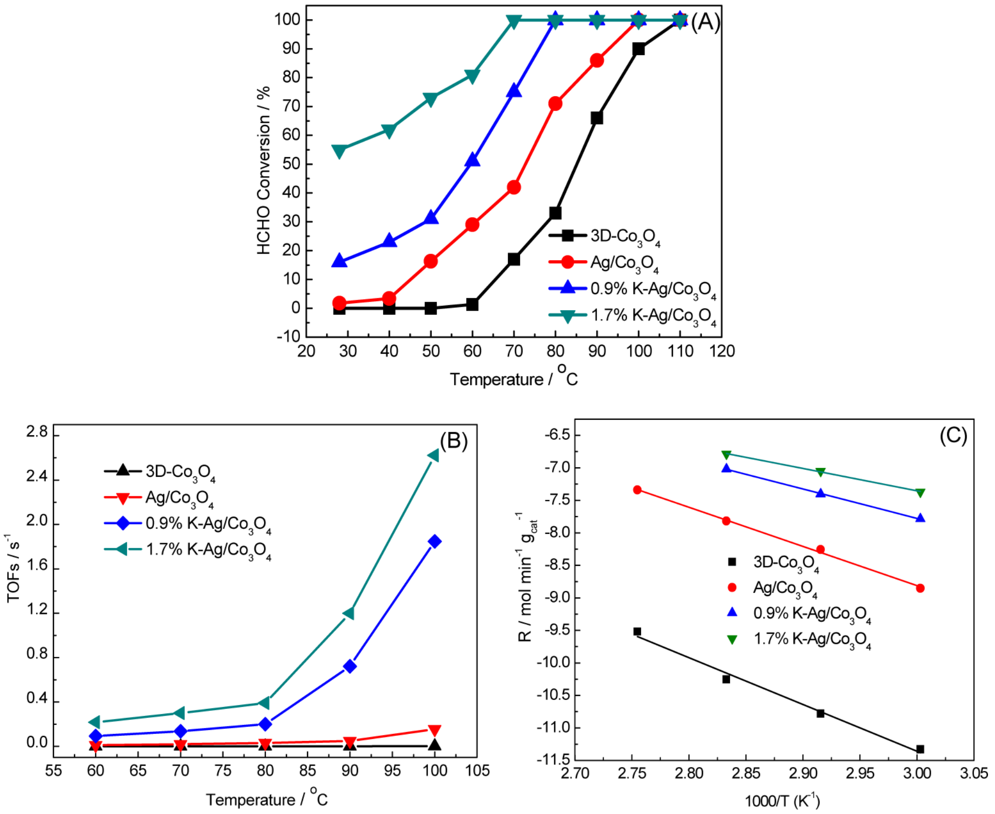

Figure 1. HCHO Conversion (A), TOFs (B), and Arrhenius plots (C) of HCHO oxidation on the samples.

Table 1. Chemical and Physical Parameter and Oxidation Activity at Room Temperature of the Different Catalysts

sample	content[a] (wt %) Ag	content[a] (wt %) K	dispersion[b] (%), D_{Ag}	particle size,[c] d_{co} (nm)	surface area (m^2/g) A_{BET}	surface area (m^2/g) A_{BJH}	pore volume, V_p (cm^3/g)	pore diameter, D_P (nm)	oxidation activity[d], conversion (%)
3D-Co_3O_4					87.8	103.2	0.210	4.3	0
Ag/Co_3O_4	8.2		29.7	3.8	59.8	35.1	0.193	1.9	2
0.9% K–Ag/Co_3O_4	6.1	0.9	13.3	8.5	67.9	41.6	0.203	1.9	16
1.7% K–Ag/Co_3O_4	6.4	1.7	8.1	13.9	64.3	38.5	0.196	1.9	55

[a] Ag and K contents obtained by ICP-OES. [b] Ag dispersion calculated by CO chemical adsorptions. [c] Average Ag particle size estimated by Ag dispersion. [d] HCHO conversion at room temperature (28 °C).

Q and HP-INNOWAX columns, respectively. No carbon products other than CO_2 were detected. The HCHO conversion was calculated from a carbon balance (i.e., 1 mol of HCHO forms 1 mol of CO_2). For kinetics measurement, the HCHO conversion is kept below 15%. Kinetics data were tested under the condition of HCHO 400 ppm and GHSV 30 000 h^{-1} for 3D-Co_3O_4, HCHO 1200 ppm and GHSV 165 000 h^{-1} for Ag/Co_3O_4 and 0.9% K–Ag/Co_3O_4, and HCHO 2000 ppm and GHSV 165 000 h^{-1} for 1.7% K–Ag/Co_3O_4. The total flows all contain 20% (vol) of O_2 and N_2 as the equilibrium gas. The HCHO conversion was calculated from the CO_2 content as follows:

$$\text{HCHO conversion (\%)} = \frac{[CO_2]_{out}}{[HCHO]_{in}} \times 100\%$$

$[CO_2]_{out}$ and $[HCHO]_{in}$ in the formula are the CO_2 concentration in the products and the HCHO concentration of the flow gas, respectively.

Turnover frequency (TOF) is defined as the number of HCHO molecules converted per surface Ag (2–1) or Co^{3+} (2–2) per second.

$$\text{turnover rate} = \frac{C_{HCHO}X_{HCHO}V_{gas}M_{Ag}}{m_{cat}w_{Ag}D_{Ag}}[s^{-1}] \tag{2-1}$$

$$\text{turnover rate} = \frac{C_{HCHO}X_{HCHO}V_{gas}}{n_{Co^{3+}}}[s^{-1}] \tag{2-2}$$

where m_{cat} is the mass of catalyst in the reactor bed; V_{gas}, the total molar flow rate; X_{HCHO}, the conversion of HCHO based on CO_2 formation; C_{HCHO}, the concentration of HCHO in gas mixture; M_{Ag}, the atomic weight of Ag; w_{Ag}, the mass fraction of silver tested by ICP-OES; D_{Ag}, the dispersion of silver estimated by CO chemical adsorption; and $n_{Co^{3+}}$, the mole number of Co^{3+} ions per gram of Co_3O_4 catalyst calculated by H_2-TPR.

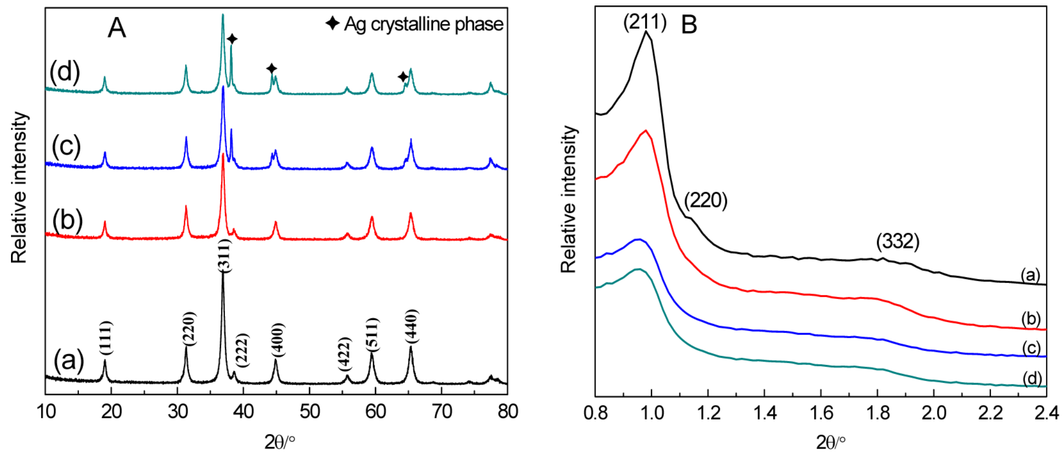

Figure 2. (A) Wide-angle and (B) low-angle XRD patterns of (a) 3D-Co_3O_4, (b) Ag/Co_3O_4, (c) 0.9% K–Ag/Co_3O_4, and (d) 1.7% K–Ag/Co_3O_4.

3. RESULTS AND DISCUSSION

3.1. Performance Test of HCHO Catalytic Oxidation.

Figure 1 shows the catalytic performance of HCHO on various catalysts. From Figure 1A, with the increase in the temperatures, the complete conversion of 3D-Co_3O_4 catalyst is dislayed at 110 °C. Ag/Co_3O_4 catalyst has better low-temperature conversion than 3D-Co_3O_4 catalyst because the addition of Ag can provide sufficient active sites for the HCHO oxidation reaction. Complete conversion of Ag/Co_3O_4 catalyst is exhibited at 100 °C. The existence of K^+ ions obviously promotes the catalytic activity of HCHO oxidation. Complete conversion of 0.9% K–Ag/Co_3O_4 is obtained at 80 °C. With the increase in the K^+ ion content, 1.7% K–Ag/Co_3O_4 catalyst shows the best catalytic performance. Its complete conversion is displayed at 70 °C. HCHO conversions of the samples at room temperature are shown in Table 1. The 1.7% K–Ag/Co_3O_4 has a better catalytic activity for HCHO oxidation (i.e., 55% of conversion at room temperature). Figure 1B displays the TOFs of Ag/Co_3O_4, 0.9% K–Ag/Co_3O_4 and 1.7% K–Ag/Co_3O_4, respectively, are 0.011, 0.092, and 0.22 s^{-1} at 60 °C and are 0.15, 1.85, and 2.62 s^{-1} at 100 °C. 3D-Co_3O_4 has a TOF of only 0.0015 s^{-1} at 100 °C due to only Co^{3+} ions as the active phase, which is calculated by the H_2 consumption of $Co^{3+} \rightarrow Co^{2+}$. The TOF of 1.7% K–Ag/$Co_3O_4$ is the largest of all the samples because of the increase in the K content. For comparison, the previously reported Ag–HMO nanorods for HCHO oxidation had a TOF of 0.006 s^{-1} at 60 °C, and the Ag/CeO_2 nanosphere had a TOF of 0.005 s^{-1} at 110 °C.[22,24] The values are much lower than the 3D mesoporous Ag/Co_3O_4 and K–Ag/Co_3O_4 catalyst. Figure 1C shows the Arrhenius plots for the rates of HCHO oxidation over the samples. The apparent activation energy of the reaction is 59.7 kJ/mol on the 3D-Co_3O_4, 50.1 kJ/mol on the Ag/Co_3O_4, 37.5 kJ/mol on the 0.9% K–Ag/Co_3O_4, and 28.5 kJ/mol on the 1.7% K–Ag/Co_3O_4. The 1.7% K–Ag/Co_3O_4 has the lowest apparent activation energy, which indicates that HCHO molecules are easily adsorbed and activated on the sample. Therefore, the addition of K^+ ions obviously promotes the catalytic performance for HCHO oxidation.

3.2. Structure Analysis.

From the wide-angle XRD patterns in Figure 2A, one can see that the catalysts have diffraction peaks at 19°, 31.3°, 36.9°, 38.2°, 44.5°, 55.6°, 59.4° and 65.3° (2θ), corresponding to the (111), (220), (311), (222), (400), (422), (511), and (440) planes.[30,40] It indicates that the samples possess the crystalline cobaltosic oxide with spinel type structure. For the K–Ag/Co_3O_4 sample, the (111), (200), and (220) facets of the Ag crystalline phases (PDF no. 65-2871), corresponding to 38.1°, 44.3°, and 64.4° (2θ), were observed. From Table 1, the Ag content of Ag/Co_3O_4 is 8.2 wt %, larger than that of K–Ag/Co_3O_4 (~6 wt %). The Ag/Co_3O_4 sample with larger Ag content does not possess the Ag phase, whereas the K–Ag/Co_3O_4 sample with a lower Ag content has the Ag phase, and the half-width of the Ag diffraction peak for K–Ag/Co_3O_4 narrows with the increase in the K^+ ions. The results indicate that the addition of K^+ ions increases the crystallite size of the Ag and decreases the Ag dispersion (Table 1). Figure 2B shows that the 3D-Co_3O_4 catalyst has the 211, 220, and 332 diffraction peaks that correspond to 1°, 1.14°, and 1.85° (2θ).[30] The 211 peak intensity decrease, and the 220 peak disappears with the addition of Ag and K, which is due to the porous regularity to be diminished. The low-angle diffraction peaks indicate that all samples are mesoporous materials with a 3D porous structure characteristic.[35]

The N_2 physical adsorption and pore size distribution patterns of the catalysts are displayed in Figure 3. All samples have type IV isotherms,[46] which indicates that the 3D mesoporous structure is not affected by Ag or K. The decrease in the hysteresis rings for Ag/Co_3O_4 and K–Ag/Co_3O_4 may be related to the decrease in the specific surface areas (Table 1). The pore size distributions of Ag/Co_3O_4 and K–Ag/Co_3O_4

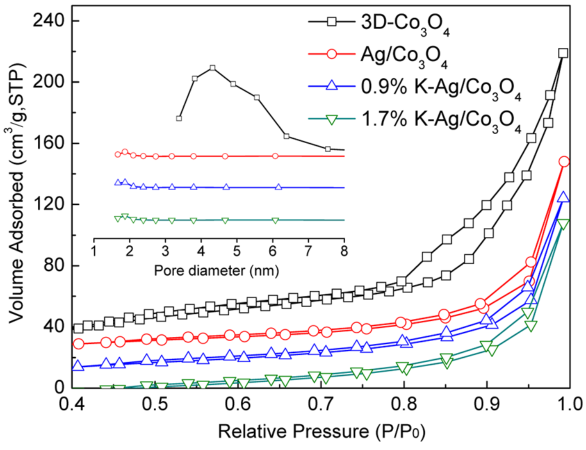

Figure 3. N_2 adsorption–desorption isotherm and pore size distributions of the catalysts.

shift to a small pore diameter field (inset, Figure 3). The maximum distribution of pore diameters for all of them is 1.9 nm. The physical parameters of the catalysts are shown in Table 1. The surface areas, pore volumes, and pore sizes of oxide-supported Ag catalysts decrease with the addition of Ag. The surface areas, pore volumes, and pore sizes are larger for the K–Ag/Co_3O_4 than for the Ag/Co_3O_4 because of the lower supported Ag content of the K–Ag/Co_3O_4.

Figure 4 clearly exhibits 3D ordered mesoporous structures of all samples. The addition of Ag does not affect the mesoporous structure of Ag/Co_3O_4 and K–Ag/Co_3O_4. The samples have uniform polycrystalline particles, and their particle sizes are ~50 nm. The particles are like the balls composed of polycrystalline pore walls and ordered pore channels. Each pore hole connects to two unlimited pore channels with different directions. It results from the KIT-6 template with a 3D symmetrical structure (ia3d).[33,35]

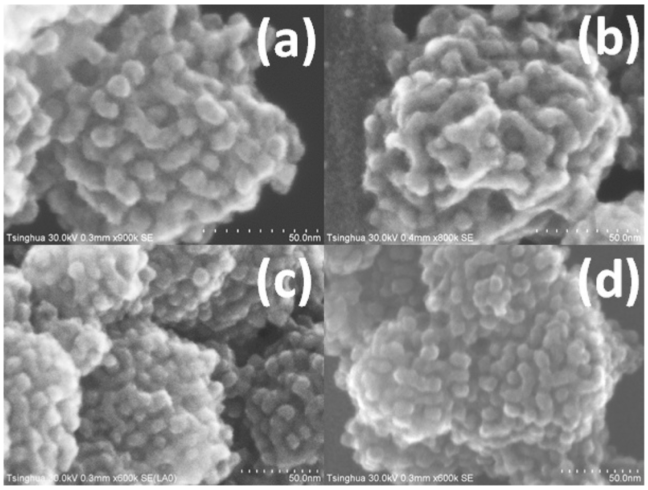

Figure 4. SEM images of (a) 3D-Co_3O_4, (b) Ag/Co_3O_4, (c) 0.9% K–Ag/Co_3O_4, and (d) 1.7% K–Ag/Co_3O_4.

TEM images of 3D-Co_3O_4, Ag/Co_3O_4, and 1.7% K–Ag/Co_3O_4 are displayed in Figure 5. All catalysts possess mesoporous characteristics and polycrystalline walls. 3D-Co_3O_4 possesses a better 3D mesoporous structure (Figure 5a) and surface lattice spacings of 0.286 and 0.467 nm for the (220) and (111) crystal planes, respectively (Figure 5b). The addition of Ag causes black spots (Figure 5c,e), which are Ag nanoparticles to be uniformly distributed on the surface of the walls. Figure 5d shows that the Ag/Co_3O_4 sample possesses (220) and (111) faces of 3D-Co_3O_4 and Ag(111) faces with a lattice spacing of 0.236 nm, respectively. Figure 5f shows that 1.7% K–Ag/Co_3O_4 exposes more Ag(111) crystal faces and no lattice fringes of 3D-Co_3O_4 present on the surface of walls. Moreover, Figure 5c,e shows that the particle size of the Ag nanoparticles is larger for 1.7% K–Ag/Co_3O_4 (about 3–22 nm) than for Ag/Co_3O_4 (about 1–10 nm). The results indicate that the addition of K^+ ions increases the particle size of the Ag nanoparticles and promotes the exposure of Ag(111) planes. For TEM, only a limited number of Ag nanoparticles can be examined. From Table 1, the average particle sizes of Ag/Co_3O_4, 0.9% K–Ag/Co_3O_4, and 1.7% K–Ag/Co_3O_4, calculated by CO chemisorptions, gradually increase with the increase in the K content, which is in agreement with the XRD results.

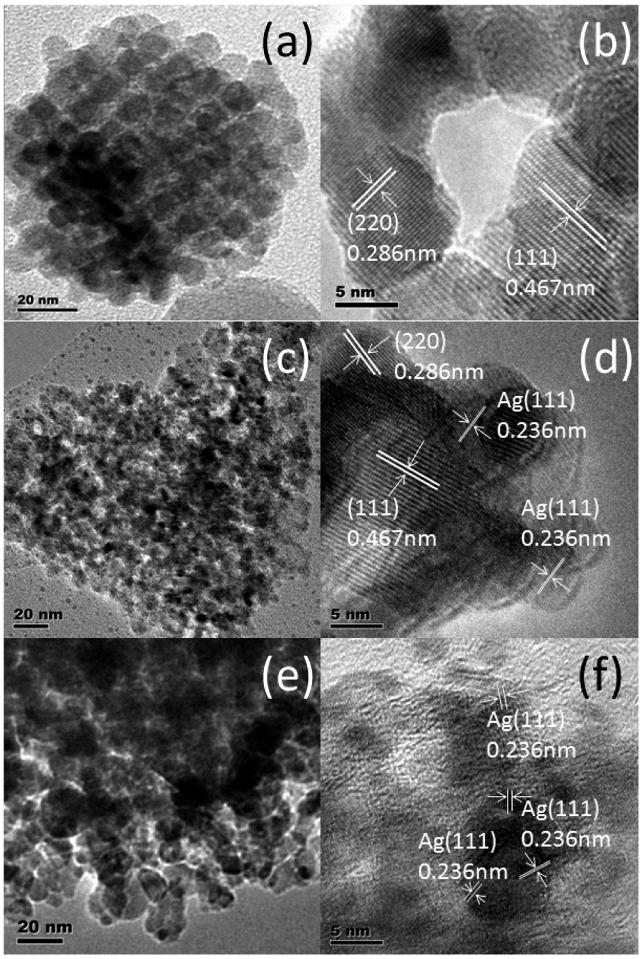

Figure 5. TEM images of (a, b) 3D-Co_3O_4, (c, d) Ag/Co_3O_4, and (e, f) 1.7% K–Ag/Co_3O_4.

3.3. Chemical Characterization. XPS patterns of the samples are displayed in Figure 6. The spectrum of Co 2p showed spin–orbit splitting into 2p1/2 and 2p3/2 components from Figure 6A. Both components contain the same qualitative information. Therefore, the higher intensity Co 2p3/2 bands were chosen to fit the curve. The Co 2p3/2 has two components at BE = 779.5 and 780.7 eV, which indicate Co^{3+} and Co^{2+} cation species, respectively.[47,48] Table 2 shows that the Co^{3+}/Co^{2+} ratios (2.7 and 2.9) of K–Ag/Co_3O_4 are more than that (2.3) of Ag/Co_3O_4 and that (2.0) of 3D-Co_3O_4, which indicates that the addition of Ag and K increases Co^{3+} ions and decreases Co^{2+} ions. For the 3D-Co_3O_4 sample, the molar ratio of Co (35.1) and O (64.9) is ~1/2, but not 3/4. This is due to the larger surface area and special pore structure of 3D-Co_3O_4, which causes the increase in the surface oxygen species.[30] In addition, from Table 2, the Ag/Co ratios of the samples decrease with the increase in the K content due to the increase in the Ag particle sizes. Figure 6B shows that O 1s has signals displayed in BE at 529.8 and 531.0 eV. The former is surface lattice oxygen (O_{latt}) species, whereas the latter is surface adsorption oxygen (O_{ads}).[11,30] From Table 2, the O_{ads}/O_{latt} ratios of Ag/Co_3O_4 (0.6) and 0.9% K–Ag/Co_3O_4 (1.1) are lower than that of 3D-Co_3O_4 (1.3); the O^{2-}/Co ratio of Ag/Co_3O_4 (1.42) and 0.9% K–Ag/Co_3O_4 (0.98) are larger than that of 3D-Co_3O_4 (0.81). The results indicate that Ag/Co_3O_4 and 0.9% K–Ag/Co_3O_4 have more abundant O^{2-} species because of the presence of Ag in the top layer. With the increase in the K^+ ion content, the O_{ads}/O_{latt} ratio increases, and the O^{2-}/Co ratio decreases for 1.7% K–Ag/Co_3O_4. It is

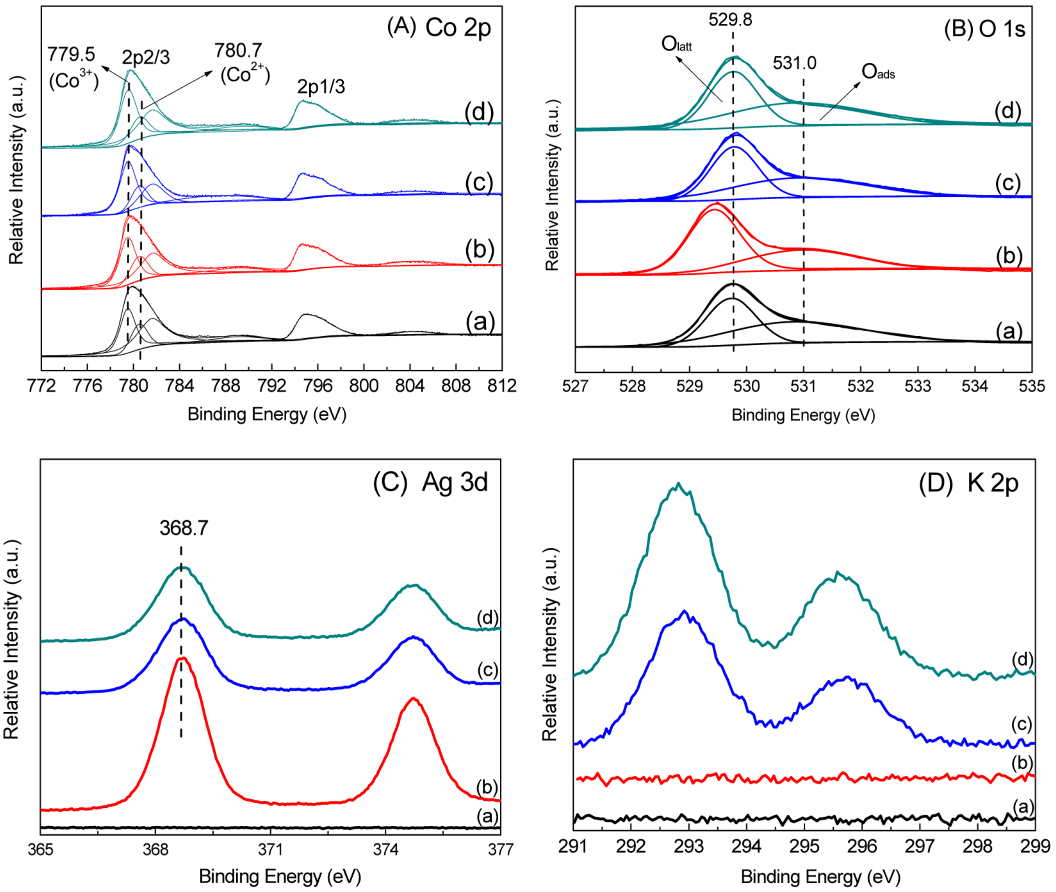

Figure 6. XPS patterns of (a) 3D-Co_3O_4, (b) Ag/Co_3O_4, (c) 0.9% K–Ag/Co_3O_4, and (d) 1.7% K–Ag/Co_3O_4.

Table 2. Surface Chemical Compositions and Element Molar Ratios of Different Catalysts

	surface element contents (at. %)				surface element molar ratios			
samples	K	Ag	Co	O	O^{2-}/Co	Ag/Co	Co^{3+}/Co^{2+}	O_{ads}/O_{latt}
3D-Co_3O_4			35.1	64.9	0.81		2.0	1.3
Ag/Co_3O_4		7.7	27.8	64.5	1.42	0.28	2.3	0.6
0.9% K–Ag/Co_3O_4	6.4	4.0	29.4	60.2	0.98	0.14	2.7	1.1
1.7% K–Ag/Co_3O_4	9.3	3.6	29.2	57.9	0.83	0.12	2.9	1.4

attributed to the existence of surface hydroxyl (OH^-) groups as O_{ads} species. In addition, the BE of O_{latt} for the Ag/Co_3O_4 sample is shifted to 529.4 eV, likely because of a greater quantity of surface lattice oxygens. From Figure 6C, Ag 3d has a signal at BE = 368.7 eV, which indicates that Ag^0 exists in the Ag/Co_3O_4 and K–Ag/Co_3O_4 samples.[22,49] It is further confirmed by TEM results. Figure 6D shows that K 2p has two components at BE = 292.8 and 295.6 eV, which confirms the existence of K^+ ions. From XPS results, it is concluded that K–Ag/Co_3O_4 possesses the Ag metallic state, abundant O^{2-} species, and a certain quantity of O_{ads} species provide by K^+ ions.

The Raman spectra of the samples are shown in Figure 7. The 3D-Co_3O_4 catalyst has five peaks at 195, 478, 518, 615, and 684 cm^{-1}, which correspond to the $F_{2g}^{(1)}$, E_g, $F_{2g}^{(2)}$, $F_{2g}^{(3)}$ and A_{1g} symmetries of Co_3O_4, respectively.[50] With the addition of Ag, the Raman peak at 684 cm^{-1} shifts to lower frequencies (675 cm^{-1}), and the peak intensities decrease. Compared with a Raman peak at 684 cm^{-1} for 3D-Co_3O_4, the peak at 666 cm^{-1} for 1.7% K–Ag/Co_3O_4 has a red shift (18 cm^{-1}). The red shift indicates that the K–Ag/Co_3O_4 catalyst causes the lattice

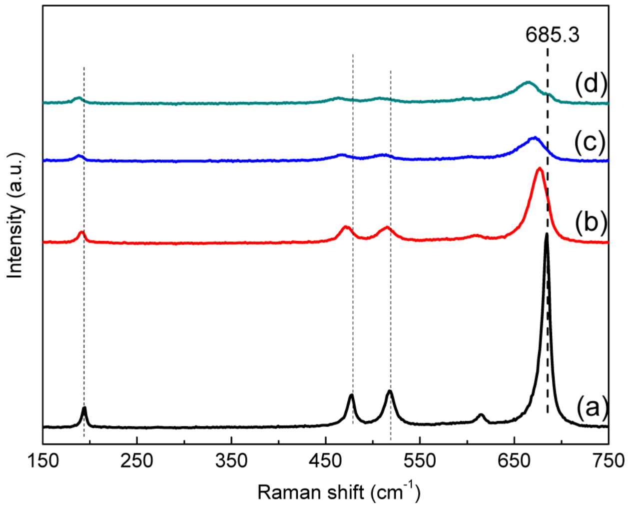

Figure 7. Raman spectra of (a) 3D-Co_3O_4, (b) Ag/Co_3O_4, (c) 0.9% K–Ag/Co_3O_4, and (d) 1.7% K–Ag/Co_3O_4.

distortion or residual stress of the spinel structure.[51,52] K–Ag/Co_3O_4 has the maximum structural defects because of not only the loading of Ag nanoparticles but also the addition of K^+ ions. The existence of lattice defects is beneficial for the formation of oxygen vacancies, which can activate, adsorb oxygen gas, and provide the lattice sites of oxygen migration.

H_2-TPR patterns of the catalysts are shown in Figure 8. From the chart, 3D-Co_3O_4 has peak 1 at 300 °C, which belongs to the reduction of Co^{3+} to Co^{2+}, and peak 2 at 362 and 419 °C, which belong to the reduction of Co^{2+} to Co^0.[30] Peaks 1 and 2 correspond to H_2 consumptions of 2.6 and 11.1 mmol/g, respectively, indicating that the Co^{3+}/Co^{2+} proportion in the sample is 0.23 (Table 3). Ag/Co_3O_4 and K–Ag/Co_3O_4 catalysts have three peaks at ~200, 300, and 342 °C, which are assigned to H_2 spillover, $Co^{3+} \rightarrow Co^{2+}$, and $Co^{2+} \rightarrow Co^0$, respectively. After addition of Ag, reduction peaks at ~300 and 340 °C show a trend to form one reduction peak attributed to the activation of surface O^{2-} species. The addition of K^+ ions enhances the reducibility and two reduction peaks at ~180 and 290 °C for the K–Ag/Co_3O_4 shift to lower temperatures, indicating the occurrence of a stronger metal–support interaction that results from H_2 spillover.[24] The H_2 spillover phenomenon exhibits an ability to adsorb, activate, and migrate hydrogen. Activated hydrogen on the Ag surface can easily migrate to the surface of the Co_3O_4 support and participate in the reduction reaction. From Table 3, peak 1 at 176 °C for 1.7% K–Ag/Co_3O_4 corresponds to a lower (2.2 mmol/g) H_2 consumption, indicating that the 1.7% K–Ag/Co_3O_4 sample possesses fewer effects of the H_2 spillover, probably because the activation of the oxygen species connecting Co^{3+} ions provides some electrons for the Ag particles. In addition, the Co^{3+}/Co^{2+} proportions in the K–Ag/Co_3O_4, calculated by the H_2 consumption ratios of peaks 2 and 3, increase with the increase in the K content. This indicates that K–Ag/Co_3O_4 has greater quantities of Co^{3+} cations, which is consistent with the XPS result. Therefore, for the K–Ag/Co_3O_4 sample, the existence of Ag enhances surface O^{2-} species, whereas the addition of K^+ ions increases Co^{3+} cations and low-temperature reducibility, resulting from the interaction between the Ag and the Co_3O_4 support. Sufficient Co^{3+} cations imply that oxygen species in the K–Ag/Co_3O_4 are easier to activate and migrate and can improve the catalytic performance of the HCHO oxidation.

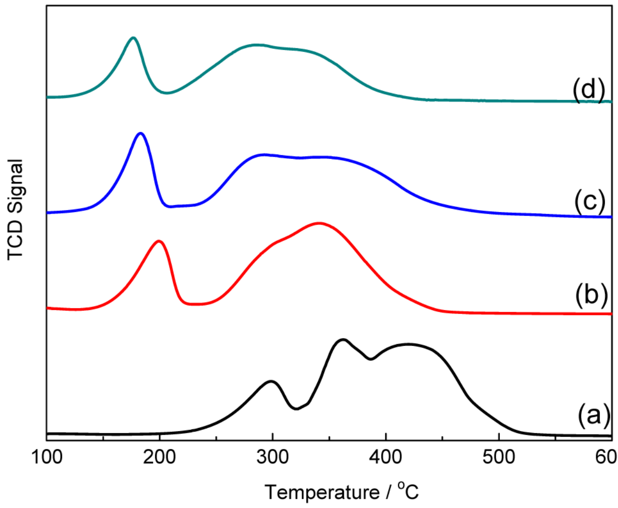

Figure 8. H_2-TPR patterns of (a) 3D-Co_3O_4, (b) Ag/Co_3O_4, (c) 0.9% K–Ag/Co_3O_4, and (d) 1.7% K–Ag/Co_3O_4.

Figure 9 shows that CO-TPD patterns of the samples, which was tested at <450 °C (calcination temperature). From the chart, all samples have desorption peaks between 50 and 200 °C that belong to the CO desorption of 3D-Co_3O_4. Ag/Co_3O_4 and K–Ag/Co_3O_4 samples have a broad desorption peak at 376 °C that belongs to the CO desorption of Ag nanoparticles. Peak intensity at 376 °C for K–Ag/Co_3O_4 decreases, indicating that the K addition reduces Ag dispersion (Table 1). The K–Ag/Co_3O_4 has a larger desorption peak between 200 and 300 °C, indicating that the addition of K^+ ions provides more abundant surface OH^- groups. The peak intensity is larger because a number of OH^- groups can react with CO to produce CO_2 and H_2. Surface OH^- species could be chemisorbed on the surface of 3D-Co_3O_4 as a result of the existence of lone electron pairs. These electrons would transfer from the O of the OH groups to Co and O of Co_3O_4. This case is similar to Na-promoted catalysts.[6,42]

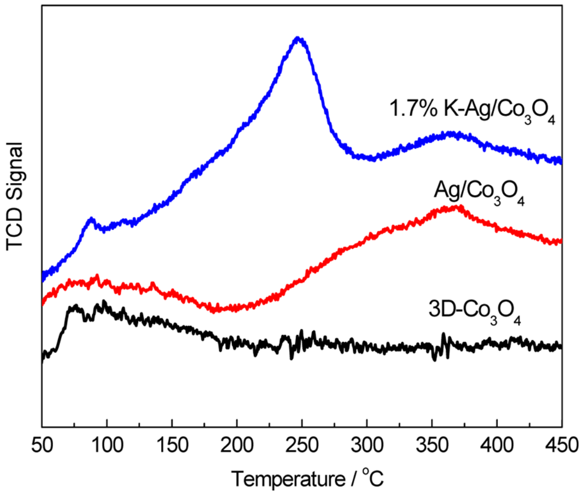

Figure 9. CO-TPD patterns of the catalysts.

Figure 10 shows the in situ DRIFTS spectra for surface species on the catalysts. From the chart, the bands appearing at 1360, 1590, 2840, and 2950 cm^{-1} are assigned to the symmetric stretch (ν_s) of COO, the asymmetric stretch (ν_{as}) of COO, the asymmetric stretch (ν_{as}) of CH, and the symmetric stretch (ν_s)

Table 3. Reduction Temperatures and H_2 Consumptions of the Catalysts

	reduction temperatures (° C)			H_2 comsumptions (mmol/g)			
samples	peak 1	peak 2	peak 3	peak 1	peak 2	peak 3	Co^{3+}/Co^{2+}
3d-Co_3O_4	300	362, 419		2.6	11.1		0.23
Ag/Co_3O_4	200	300	342	2.8	2.2	7.1	0.31
0.9% K–Ag/Co_3O_4	183	292	346	2.8	4.0	5.2	0.77
1.7% K–Ag/Co_3O_4	176	284	322	2.2	4.2	2.5	1.68

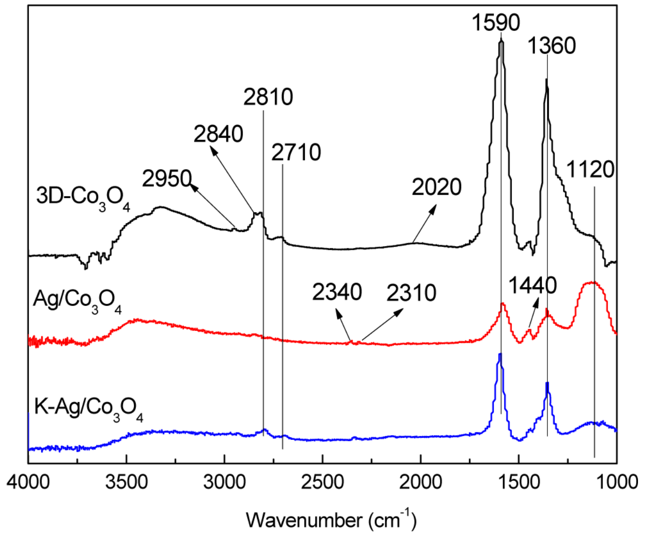

Figure 10. In situ DRIFTS spectra of the catalysts.

of the CH of formate, respectively. The bands observed at 2340 and 2310 cm^{-1} are ascribed to the CO_2 stretch in the gas phase.[19,40] The peaks at 1440, 2710, and 2810 cm^{-1} probably belong to the CH bending vibration, the asymmetric CH stretch (ν_{as}) and the symmetric CH stretch (ν_s) of dioxymethylene. HCHO easily forms dioxymethylene in the presence of oxygen. The bands appearing at 1120 cm^{-1} should be due to the ν CO stretch of dioxymethylene.[23] The peaks at 2023 cm^{-1} are due to the adsorption of carbon monoxide.[6] Broad peaks between 3000 and 3500 cm^{-1} can be attributed to the isolated and combined OH^- species.

According to the DRIFTS results, the formate adsorbed species and OH^- species on the surface of 3D-Co_3O_4 are more abundant than on the surface of Ag/Co_3O_4 and K–Ag/Co_3O_4, and the surface of 3D-Co_3O_4 contains CO adsorbed species. It indicates that a great number of HCHO molecules are adsorbed on the surface of 3D-Co_3O_4 and form formate species. Then the formate species break up into CO and OH^- species. The addition of Ag increases the ν CO stretch of dioxymethylene and CO_2 adsorbed species (2310 and 2340 cm^{-1}); reduces formate species, which can demostrate that HCHO molecules are more easily adsorbed on the catalysts because of the existence of Ag nanoparticles and are converted into much more dioxymethylene species on the surface of Ag/Co_3O_4. Fewer dioxymethylene species further form formate species, which are decomposed into CO and OH^- species. Then the CO species are oxidized by active oxygen species (O*) to form CO_2. Compared with the Ag/Co_3O_4, much less OH^- and dioxymethylene species exist on the surface of the K–Ag/Co_3O_4 catalyst in the reaction process. It can infer that most dioxymethylene species are converted to formate species, which can directly react with surface OH^- species to produce CO_2 and H_2O. Consumed OH^- species could be supplemented by O^{2-} species, which are generated through the interaction of Ag and Co.

3D-Co_3O_4 catalyst as a support has a special pore structure and larger surface area, which are conducive to the diffusion of reactants and products and the exposure of the active phase.[30] Usually, sufficient Ag active sites and O^{2-} species exist in the oxide-supported Ag catalysts, which can enhance the catalytic performance at low temperature.[22,23,47] The Ag/Co_3O_4 and K–Ag/Co_3O_4 samples possess more abundant O^{2-} species from XPS and H_2-TPR results, which are favorable for the adsorption and activation of HCHO molecules. From XRD and TEM results, the K–Ag/Co_3O_4 with less Ag content obviously has larger Ag particles and exposes more Ag(111) crystal facets because of the K^+ addition, both of which are related to the interaction of Ag with Co. H_2-TPR results confirm that a stronger metal–support interaction improves the low-temperature reducibility of K–Ag/Co_3O_4, implying that oxygen species of the K–Ag/Co_3O_4 are more easily desorbed and react with hydrogen because of K^+ ions. Raman results confirm that the K–Ag/Co_3O_4 has the maximum structural defects, which are beneficial to formation of oxygen vacancies. In the K–Ag/Co_3O_4 catalyst, the formation of oxygen vacancies is related to a large quantity of Co^{3+} cations. Xie et al.[53] reported that CO molecules can be easily oxidized by the more active Co^{3+} cations on the (110) faces of a Co_3O_4 nanorod, which is the active species of the oxidation reaction. More Co^{3+} cations species can increase oxygen vacancy densities, which result from anion structural defects. The oxygen vacancies directly participate in the adsorption, activation, and migration of oxygen (see Figure 11). CO-TPD results demonstrate the existence of surface OH^- and the adsorption ability of K–Ag/Co_3O_4. Thus, the addition of K^+ ions into Ag/Co_3O_4 promotes interaction of Ag with Co, strengthens lattice defects, and leads to the exposure of Ag(111) faces and an increase in Co^{3+} cations.

In actual fact, the Ag(111) crystal facets, Co^{3+} ions, and surface lattice oxygen of K–Ag/Co_3O_4 are all involved in the process of the oxidation reaction. The Ag(111) planes are active faces of HCHO oxidation and could activate the O^{2-} species of 3D-Co_3O_4. The O^{2-} species could also improve the reaction ability of the Ag(111) surface; enhance the breakage of H_2, O_2, and NO bonds; and strengthen the bonding ability of H, O, N, and C atoms to the Ag(111) surface.[54] In the process of the reaction, the active O^{2-} species around Ag are directly depleted and replenished by Co_3O_4 support as a reservoir

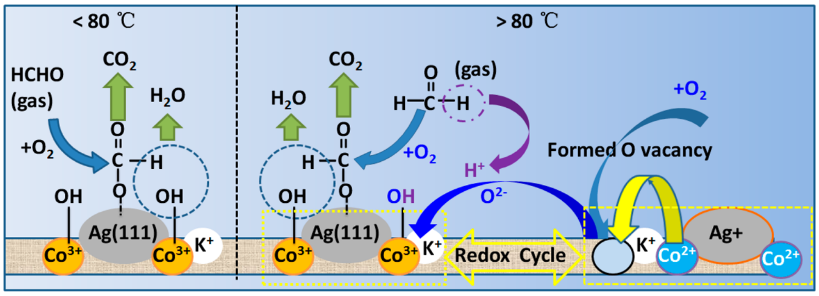

Figure 11. Reaction pathway of the K–Ag/Co_3O_4 catalyst.

providing oxygen.[55] The activation and migration of oxygen species on the oxygen vacancies are dependent on the redox cycles of Co^{3+}/Co^{2+} and Ag^+/Ag^0 after the O^{2-} species are consumed (see Figure 11, the yellow line box).[53,56] The redox cycle is possibly the same as the redox cycles of Mn^{4+}/Mn^{3+} and Ce^{4+}/Ce^{3+}.[3] The increase in Co^{3+} ions is much more favorable for the formation of oxygen vacancies,[53] which can enhance the redox cycles of Co^{3+}/Co^{2+} and Ag^+/Ag^0.

In addition, owing to the addition of K^+ ions, the K–Ag/Co_3O_4 catalyst exhibits surface adsorbed oxygen species, which are identified as surface OH^- species from the CO-TPD results. Surface OH^- species play a critical role on the reaction path of HCHO oxidation. The CO-TPD results demonstrate that the surface OH^- species can easily adsorb CO species at low temperatures. A surface OH^- can immediately react with formate species on the surface of K–Ag/Co_3O_4 to form a molecule of CO_2 and H_2O, which is similar to the reaction path of the Na–Pt/TiO_2 catalyst.[6] The difference is that the O^{2-} species at the perimeter of Ag in the K–Ag/Co_3O_4 catalyst participate in the oxidation reaction of HCHO because of the stronger interaction of Ag with Co and anion lattice defects. Compared with Ag/Co_3O_4, the TOFs of K–Ag/Co_3O_4, especially 1.7% K–Ag/Co_3O_4, are much higher. We believe that at low temperature (<80 °C), the HCHO catalytic activity on the K–Ag/Co_3O_4 catalyst depends to a large extent on the surface OH^- species at the perimeter of Ag(111) facets; at relatively high temperature (>80 °C), the surface OH^- species are consumed and replaced quickly, and their supplement relies on the migration of O^{2-} species from the 3D-Co_3O_4 support. Figure 11 clearly exhibits the reaction process. Thus, the pathway of reaction for HCHO oxidation on the K–Ag/Co_3O_4 follows the HCHO → $CHOO^-$ + OH^- → CO_2 + H_2O route. For Ag/Co_3O_4, the reaction path follows the HCHO → $CHOO^-$ → CO + O* → CO_2 route. The O^{2-} species play an important role in the oxidation reaction, and these active O* species often cause the complex migration though oxygen vacancies to occur.[57−59] On the basis of the TOFs of Ag/Co_3O_4, the catalytic activity is dependent on the O^{2-} species around Ag nanoparticles at low temperature (<90 °C) and relies on the O^{2-} species at the perimeter of the Ag that migrate from the 3D-Co_3O_4 support at relatively high temperature (>90 °C).

4. CONCLUSION

In summary, 3D mesoporous Ag/Co_3O_4 and K–Ag/Co_3O_4 catalysts were prepared on the basis of 3D-Co_3O_4. Ag nanoparticles are uniformly distributed on the polycrystalline pore walls. The addition of Ag nanoparticles and K^+ ions does not affect the mesoporous structure and only decreases the surface areas, pore diameters, and pore volumes. Compared with Ag/Co_3O_4, the TOF of K–Ag/Co_3O_4 is much higher, which is attributed to more abundant surface OH^- species provided by K^+ ions, Ag(111) active faces, Co^{3+} ions, and O^{2-} species that result from interaction of the Ag with Co and anion lattice defects. Ag(111) faces are active planes; surface OH^- and O^{2-} are active species. At low temperature (<80 °C), the HCHO catalytic activity on the K–Ag/Co_3O_4 catalyst depends to a large extent on the surface OH^- species around the Ag(111) facets: at relatively high temperature (>80 °C), the surface OH^- species are consumed and replaced quickly, and their supplement relies on the migration of O^{2-} species from the 3D-Co_3O_4 support. This conclusion can help one to understand the reason for the K-promoted catalytic activity.

■ AUTHOR INFORMATION

Corresponding Author

*Phone: +86 10 62771093. Fax: +86 10 62771093. E-mail: lijunhua@tsinghua.edu.cn.

Notes

The authors declare no competing financial interest.

■ ACKNOWLEDGMENTS

This study was supported by the State Environmental Protection Key Laboratory of Sources and Control of Air Pollution Complex. This work was also supported by the National Natural Science Fund of China (Grants Nos. 21325731, 21221004) and the National High Science & Technology Project of China (Grant No. 2013AA065304).

■ REFERENCES

(1) Salthammer, T.; Mentese, S.; Marutzky, R. *Chem. Rev.* **2010**, *110* (4), 2536−2572.

(2) Quiroz Torres, J.; Royer, S.; Bellat, J. P.; Giraudon, J. M.; Lamonier, J. F. *ChemSusChem* **2013**, *6* (4), 578−592.

(3) Tang, X.; Chen, J.; Huang, X.; Xu, Y.; Shen, W. *Appl. Catal., B* **2008**, *81* (1−2), 115−121.

(4) Kim, S. S.; Park, K. H.; Hong, S. C. *Appl. Catal., A* **2011**, *398* (1−2), 96−103.

(5) Huang, H.; Leung, D. Y. C. *J. Catal.* **2011**, *280* (1), 60−67.

(6) Zhang, C.; Liu, F.; Zhai, Y.; Ariga, H.; Yi, N.; Liu, Y.; Asakura, K.; Flytzani-Stephanopoulos, M.; He, H. *Angew. Chem., Int. Ed.* **2012**, *51* (38), 9628−32.

(7) Zhang, C.; He, H.; Tanaka, K. *Appl. Catal., B* **2006**, *65* (1−2), 37−43.

(8) Yu, X.; He, J.; Wang, D.; Hu, Y.; Tian, H.; He, Z. *J. Phys. Chem. C* **2011**, *116* (1), 851−860.

(9) An, N.; Yu, Q.; Liu, G.; Li, S.; Jia, M.; Zhang, W. *J. Hazard. Mater.* **2011**, *186* (2−3), 1392−1397.

(10) An, N.; Zhang, W.; Yuan, X.; Pan, B.; Liu, G.; Jia, M.; Yan, W.; Zhang, W. *Chem. Eng. J.* **2013**, *215−216* (0), 1−6.

(11) Huang, H.; Leung, D. Y. C. *ACS Catal.* **2011**, *1* (4), 348−354.

(12) Park, S. J.; Bae, I.; Nam, I. S.; Cho, B. K.; Jung, S. M.; Lee, J. H. *Chem. Eng. J.* **2012**, *195−196* (0), 392−402.

(13) O'Shea, V. A. d. l. P.; Álvarez-Galván, M. C.; Fierro, J. L. G.; Arias, P. L. *Appl. Catal., B* **2005**, *57* (3), 191−199.

(14) Shen, Y.; Yang, X.; Wang, Y.; Zhang, Y.; Zhu, H.; Gao, L.; Jia, M. *Appl. Catal., B* **2008**, *79* (2), 142−148.

(15) Li, H. F.; Zhang, N.; Chen, P.; Luo, M. F.; Lu, J. Q. *Appl. Catal., B* **2011**, *110* (0), 279−285.

(16) Liu, B. C.; Li, C. Y.; Zhang, Y. F.; Liu, Y.; Hu, W. T.; Wang, Q.; Han, L.; Zhang, J. *Appl. Catal., B* **2012**, *111*, 467−475.

(17) Li, C.; Shen, Y.; Jia, M.; Sheng, S.; Adebajo, M. O.; Zhu, H. *Catal. Commun.* **2008**, *9* (3), 355−361.

(18) Zhang, Y.; Shen, Y.; Yang, X.; Sheng, S.; Wang, T.; Adebajo, M. F.; Zhu, H. *J. Mol. Catal. A: Chem.* **2010**, *316* (1−2), 100−105.

(19) Ma, C.; Wang, D.; Xue, W.; Dou, B.; Wang, H.; Hao, Z. *Environ. Sci. Technol.* **2011**, *45* (8), 3628−3634.

(20) Liu, B. C.; Liu, Y.; Li, C. Y.; Hu, W. T.; Jing, P.; Wang, Q.; Zhang, J. *Appl. Catal., B* **2012**, *127*, 47−58.

(21) Qu, Z. P.; Shen, S. J.; Chen, D.; Wang, Y. *J. Mol. Catal. A: Chem.* **2012**, *356*, 171−177.

(22) Huang, Z.; Gu, X.; Cao, Q.; Hu, P.; Hao, J.; Li, J.; Tang, X. *Angew. Chem., Int. Ed.* **2012**, *51* (17), 4198−4203.

(23) Mao, C. F.; Vannice, M. A. *J. Catal.* **1995**, *154* (2), 230−244.

(24) Ma, L.; Wang, D.; Li, J.; Bai, B.; Fu, L.; Li, Y. *Appl. Catal., B* **2014**, *148−149* (0), 36−43.

(25) Tang, X.; Chen, J.; Li, Y.; Li, Y.; Xu, Y.; Shen, W. *Chem. Eng. J.* **2006**, *118* (1−2), 119−125.

(26) Chen, H.; He, J.; Zhang, C.; He, H. *J. Phys. Chem. C* **2007**, *111* (49), 18033−18038.

(27) Bai, L.; Wyrwalski, F.; Lamonier, J. F.; Khodakov, A. Y.; Monflier, E.; Ponchel, A. *Appl. Catal., B* **2013**, *138−139* (0), 381−390.

(28) Wang, Y.; Zhu, A.; Chen, B.; Crocker, M.; Shi, C. *Catal. Commun.* **2013**, *36* (0), 52−57.

(29) Xia, Y.; Dai, H.; Zhang, L.; Deng, J.; He, H.; Au, C. T. A. *Appl. Catal., B* **2010**, *100* (1−2), 229−237.

(30) Bai, B.; Arandiyan, H.; Li, J. *Appl. Catal., B* **2013**, *142−143* (0), 677−683.

(31) Lee, B.; Lu, D.; Kondo, J. N.; Domen, K. *J. Am. Chem. Soc.* **2002**, *124* (38), 11256−11257.

(32) Ren, Y.; Ma, Z.; Bruce, P. G. *Chem. Soc. Rev.* **2012**, *41* (14), 4909−4927.

(33) Jiao, F.; Hill, A. H.; Harrison, A.; Berko, A.; Chadwick, A. V.; Bruce, P. G. *J. Am. Chem. Soc.* **2008**, *130* (15), 5262−5266.

(34) Jiao, K.; Zhang, B.; Yue, B.; Ren, Y.; Liu, S.; Yan, S.; Dickinson, C.; Zhou, W.; He, H. *Chem. Commun.* **2005**, *0* (45), 5618−5620.

(35) Tüysüz, H.; Lehmann, C. W.; Bongard, H.; Tesche, B.; Schmidt, R.; Schüth, F. *J. Am. Chem. Soc.* **2008**, *130* (34), 11510−11517.

(36) Xiao, J.; Frauenheim, T. *J. Phys. Chem. C* **2012**, *117* (4), 1804−1808.

(37) Zhang, X.; Wang, H.; Xu, B. Q. *J. Phys. Chem. B* **2005**, *109* (19), 9678−9683.

(38) Liu, L.; Gu, X.; Cao, Y.; Yao, X.; Zhang, L.; Tang, C.; Gao, F.; Dong, L. *ACS Catal.* **2013**, *3* (12), 2768−2775.

(39) An, K.; Alayoglu, S.; Musselwhite, N.; Plamthottam, S.; Melaet, G.; Lindeman, A. E.; Somorjai, G. A. *J. Am. Chem. Soc.* **2013**, *135* (44), 16689−16696.

(40) Ma, C. Y.; Mu, Z.; Li, J. J.; Jin, Y. G.; Cheng, J.; Lu, G. Q.; Hao, Z. P.; Qiao, S. Z. *J. Am. Chem. Soc.* **2010**, *132* (8), 2608−2613.

(41) Liu, Y.; Dai, H.; Deng, J.; Xie, S.; Yang, H.; Tan, W.; Han, W.; Jiang, Y.; Guo, G. *J. Catal.* **2014**, *309* (0), 408−418.

(42) Nie, L.; Yu, J.; Li, X.; Cheng, B.; Liu, G.; Jaroniec, M. *Environ. Sci. Technol.* **2013**, *47* (6), 2777−2783.

(43) Avgouropoulos, G.; Oikonomopoulos, E.; Kanistras, D.; Ioannides, T. *Appl. Catal., B* **2006**, *65* (1−2), 62−69.

(44) Malet, P.; Caballero, A. *J. Chem. Soc., Faraday Trans.* **1988**, *84* (7), 2369−2375.

(45) Monti, M. A. D.; Baiker, A. *J. Catal.* **1983**, *83*, 323−335.

(46) Rumplecker, A.; Kleitz, F.; Salabas, E. L.; Schüth, F. *Chem. Mater.* **2007**, *19* (3), 485−496.

(47) Zhu, Z.; Lu, G.; Zhang, Z.; Guo, Y.; Guo, Y.; Wang, Y. *ACS Catal.* **2013**, *3* (6), 1154−1164.

(48) Biesinger, M. C.; Payne, B. P.; Grosvenor, A. P.; Lau, L. W. M.; Gerson, A. R.; Smart, R. S. C. *Appl. Surf. Sci.* **2011**, *257* (7), 2717−2730.

(49) Zhang, G.; Zheng, L.; Zhang, M.; Guo, S.; Liu, Z. H.; Yang, Z.; Wang, Z. *Energy Fuels* **2011**, *26*, 618−623.

(50) Liu, Q.; Wang, L. C.; Chen, M.; Cao, Y.; He, H.-Y.; Fan, K. N. *J. Catal.* **2009**, *263* (1), 104−113.

(51) Lou, Y.; Wang, L.; Zhao, Z.; Zhang, Y.; Zhang, Z.; Lu, G.; Guo, Y.; Guo, Y. *Appl. Catal., B* **2014**, *146* (0), 43−49.

(52) Lopes, I.; El Hassan, N.; Guerba, H.; Wallez, G.; Davidson, A. *Chem. Mater.* **2006**, *18* (25), 5826−5828.

(53) Xie, X. W.; Li, Y.; Liu, Z. Q.; Haruta, M.; Shen, W. J. *Nature* **2009**, *458* (7239), 746−749.

(54) Xu, Y.; Greeley, J.; Mavrikakis, M. *J. Am. Chem. Soc.* **2005**, *127*, 12823−12827.

(55) Xu, R.; Wang, X.; Wang, D.; Zhou, K.; Li, Y. *J. Catal.* **2006**, *237* (2), 426−430.

(56) Xia, G. G.; Yin, Y. G.; Willis, W. S.; Wang, J. Y.; Suib, S. L. *J. Catal.* **1999**, *185*, 91−105.

(57) Wittstock, A.; Zielasek, V.; Biener, J.; Friend, C. M.; Bäumer, M. *Science* **2010**, *327*, 319−322.

(58) Over, H.; Seitsonen, A. P. *Science* **2002**, *297*, 2003−2005.

(59) Lei, Y.; Mehmood, F.; Lee, S.; Greeley, J.; Lee, B.; Seifert, S.; Winans, R. E.; Elam, J. W.; Meyer, R. J.; Redfern, P. C.; Teschner, D.; Schlögl, R.; Pellin, M. J.; Curtiss, L. A.; Vajda, S. *Science* **2010**, *328*, 224−228.